Hollow ZnO Nanofibers Fabricated Using Electrospun Polymer Templates and Their Electronic Transport Properties

Seung-Hoon Choi,[†,‡] Guy Ankonina,[§] Doo-Young Youn,[†] Seong-Geun Oh,[‡] Jae-Min Hong[†] Avner Rothschild,[§,*] and Il-Doo Kim[†,*]

[†]Center for Energy Materials Research, Korea Institute of Science and Technology, PO Box 131, Cheongryang, Seoul, Republic of Korea, [‡]Department of Chemical Engineering, Hanyang University, Hangdang-dong, Seoul, Republic of Korea, and [§]Faculty of Materials Engineering, Technion—Israel Institute of Technology, Technion City, Haifa 32000, Israel

ABSTRACT Thin (0.5 to 1 μm) layers of nonaligned or quasi-aligned hollow ZnO fibers were prepared by sputtering ZnO onto sacrificial templates comprising polyvinyl-acetate (PVAc) fibers deposited by electrospinning on silicon or alumina substrates. Subsequently, the ZnO/PVAc composite fibers were calcined to remove the organic components and crystallize the ZnO overlayer, resulting in hollow fibers comprising nanocrystalline ZnO shells with an average grain size of 23 nm. The inner diameter of the hollow fibers ranged between 100 and 400 nm and their wall thickness varied from 100 to 40 nm from top to bottom. The electronic transport and gas sensing properties were examined using DC conductivity and AC impedance spectroscopy measurements under exposure to residual concentrations (2−10 ppm) of NO_2 in air at elevated temperatures (200−400 °C). The inner and outer surface regions of the hollow ZnO fibers were depleted of mobile charge carriers, presumably due to electron localization at O^- adions, constricting the current to flow through their less resistive cores. The overall impedance comprised interfacial and bulk contributions. Both contributions increased upon exposure to electronegative gases such as NO_2 but the bulk contribution was more sensitive than the interfacial one. The hollow ZnO fibers were much more sensitive compared to reference ZnO thin film specimens, displaying even larger sensitivity enhancement than the 2-fold increase in their surface to volume ratio. The quasi-aligned fibers were more sensitive than their nonaligned counterparts.

KEYWORDS: hollow fibers · nanofibers · nanotubes · thin films · ZnO · electrospinning · sputtering · fiber alignment · sacrificial templates · gas sensors · impedance spectroscopy

In recent years, hollow nanomaterials such as metal−oxide nanotubes or hollow spheres have been explored worldwide for potential application as functional elements in chemical[1] and gas sensors,[2−4] catalysts,[5] dye sensitized solar cells,[6,7] photoelectrochemical cells,[8] and electrodes for supercapacitors[9] and biomolecular devices.[10] The widespread interest in these materials arises from their unique electrical, electrochemical, and catalytic properties which are closely tied to their high surface-to-volume ratio and, in some cases, unusual transport properties connected with confinement effects, one-dimensional (1D) transport phenomena, or transport in fractal dimensions. Different approaches have been developed to fabricate device architectures whose building blocks comprise nanosized hollow spheres,[11] hemispheres,[12] nanocubes,[13] or nanotubes.[14] The primary synthesis methods to date have been anodic oxidation to produce metal−oxide nanotubes[14] and chemical or physical deposition on sacrificial colloidal templates to prepare 2D or 3D arrays of hollow spheres.[3,4,11] Despite the intensive research activity in this field over the past few years, developing innovative fabrication methods that provide versatility in materials selection as well as structural and dimensional flexibility and control remains a key challenge toward device applications.

In this work we present a new processing strategy for the fabrication of unique device architectures comprising hollow fibers of inorganic materials with typical length of up to several centimeters, submicrometer diameter, and wall thickness of several tens of nanometers. These hollow fibers can be assembled in different ways enabling to construct nanoengineered device architectures with tailored functional properties. We demonstrate application of this fabrication method as a means to produce highly sensitive chemical sensors comprising hollow fibers of ZnO, an important material with potential applications in electronic and optoelectronic devices.[15] Random (nonaligned) or quasi-aligned fibers were obtained by modifying process parameters, demonstrating some of the fascinating opportunities offered by our

*Address correspondence to idkim@kist.re.kr, avnerrot@technion.ac.il.

Received for review February 8, 2009 and accepted August 10, 2009.

Published online August 17, 2009. 10.1021/nn900126k CCC: $40.75

© 2009 American Chemical Society

fabrication method for device engineering at the nanoscale. The electronic transport properties were examined using DC conductivity and AC impedance spectroscopy measurements, enabling a discernment between the contributions of surface and bulk parallel conduction paths along the fibers to the overall impedance of the specimen.

Our fabrication method involves electrospinning of polymer fibers that serve as sacrificial templates for subsequent physical vapor deposition (PVD) of inorganic materials such as metal−oxides or metals in the form of thin overlayers that coat the fibers. Finally, the polymer template is decomposed by calcination, leaving hollow fibers of the inorganic shells. Among the different strategies for producing fibers of organic or inorganic materials, electrospinning offers several advantages including ease of fabrication and versatility.[16,17] Over 20 different metal−oxides including lead zirconate (PZT), mesoporous TiO_2, and two-phase mixtures of NiO/ZnO and other couples have been prepared in this way.[18] Long continuous fibers with submicrometer diameter can be produced, with potential for alignment and spooling. Different fiber morphologies can be obtained *via* control of the processing conditions, enabling the production of dense as well as hollow, porous, and core−shell structures.[19] Near-field electrospinning techniques are being developed as a potential tool for direct write nanofabrication of various materials.[20] Recently, there have been a few reports on the application of electrospun polymer fibers as sacrificial templates for preparing inorganic hollow fibers in which the inorganic shells were deposited onto the polymer templates by means of chemical vapor deposition (CVD)[21] or electroless plating methods,[22] but their functional properties and prospective application in nanoelectronic devices remain unexplored up until now.

RESULTS AND DISCUSSION

The processing steps of our fabrication procedure are shown schematically in Figure 1. Polyvinyl-acetate (PVAc) fibers were electrospun onto silicon or alumina substrates, serving as sacrificial templates onto which ZnO overlayers were sputtered subsequently. In general, nonaligned fibers in the form of nonwoven mats are obtained in conventional electrospinning as a result of the chaotic motion (resulting from bending instability) of the polymer fiber injected from the nozzle, as shown in Figure 1a.[16] In order to align the fibers in parallel to each other along some axis, two stripes of aluminum wires were placed along opposite edges of the substrate and connected to the ground terminal of the power supply that applied the electrical field between the nozzle and the substrate during the electrospinning processes. This imposed a directional distribution of the electrical field flux lines between the nozzle and the aluminum wires, as depicted in Figure 1b, facilitating alignment of segments of the fibers across the aluminum wires.[23] The difference between the nonaligned and quasi-aligned PVAc fibers is clearly observed in the scanning electron microscopy (SEM) micrographs in Figure 2a (left and right micrographs, respectively).

Following the electrospinning process a thin overlayer of ZnO was sputtered onto the PVAc fiber template covering the substrate. Subsequently, the specimen was calcined at 500 °C for 1 h to remove the polymer template by thermal decomposition of the organic components and crystallize the inorganic (ZnO) overlayer. Thermogravimetric measurements showed no weight loss during 1 h anneal at 500 °C, and elemental analysis showed negligibly small (~0.25 wt %) amount of carbonaceous residues in the calcined specimens, indicating that the organic components completely degraded to volatile specie during the calcination step. As a result, ZnO replicas of the PVAc fibers were produced in the form of hollow fibers having inner diameter ranging between 100 and 400 nm and asymmetric wall thickness varying from approximately 100 to 40 nm from top to bottom. The asymmetrical wall thickness arises from shadowing effects as dis-

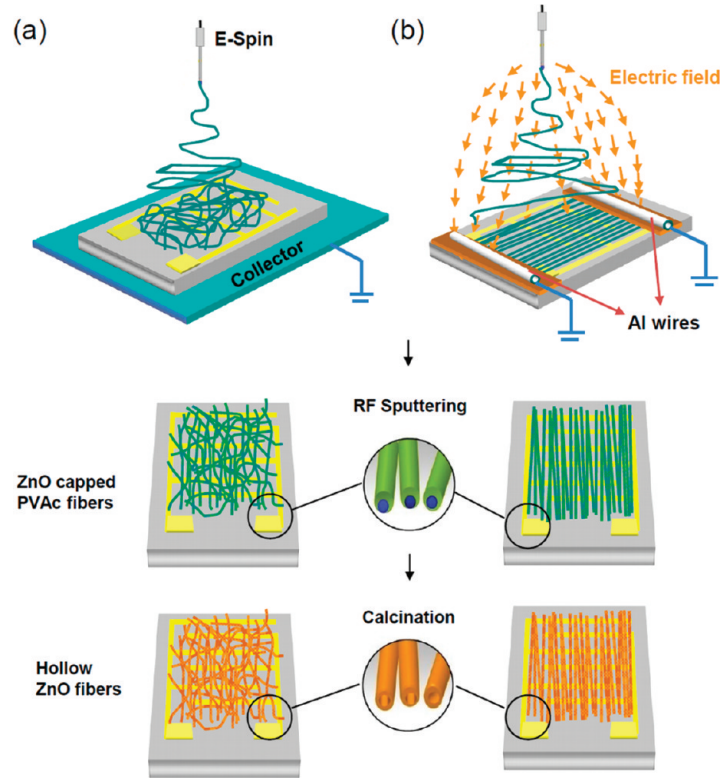

Figure 1. Schematic diagram illustrating the fabrication procedure of an array of nonaligned (a) or quasi-aligned hollow ZnO fibers (b).

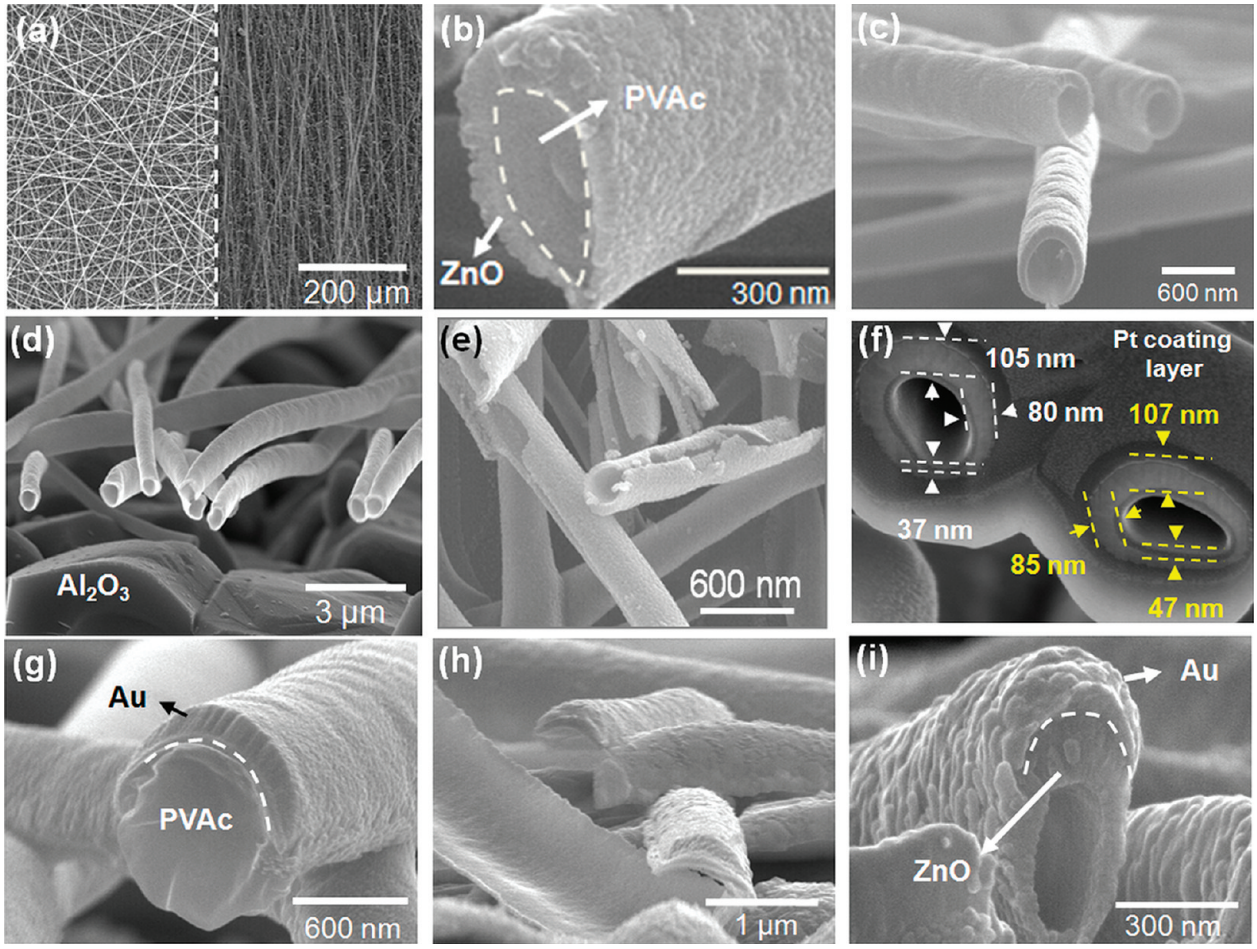

Figure 2. SEM micrographs of (a) as-spun PVAc fibers (left, nonaligned; right, quasi-aligned); (b) close-up image from a broken part of the fiber showing the as-deposited ZnO overlayer coating the electrospun PVAc fiber; (c) high magnification image of hollow ZnO fibers after calcination at 500 °C; (d) tilted view image of quasi-aligned hollow ZnO fibers; (e) cracks at the bottom of ZnO fibers that have been scratched from the substrate; (f) FIB cross section image of hollow ZnO fibers; (g) tilted view image of a broken part of a PVAc fiber coated with thermally evaporated gold overlayer in the as-deposited state; (h) tilted view image of bended belt-shaped broken fragments of the gold overlay after calcination at 500 °C; (i) close-up cross sectional image of a hollow ZnO fiber with a gold crust on top of it (after calcination at 500 °C).

cussed below. The inner diameter and wall thickness can be tuned by tailoring the electrospinning and sputtering processes, respectively. Cracks were formed at the bottom of the ZnO fibers, most likely due to high pressure that built up in the core of the fibers as the organic components decomposed.

Exemplary SEM micrographs showing typical fiber morphologies are depicted in Figure 2. Figure 2a shows nonaligned (left image) and quasi-aligned PVAc fibers (right image) in the as-spun state. The fiber diameter ranged between 200 and 500 nm. The thickness of the PVAc fiber mats scales with the amount of polymer solution electrospun onto the substrate. The layers produced and investigated in this work were approximately 0.5−1 μm thick. Figure 2b shows a high magnification SEM image of a composite fiber prior to the calcination step. It comprises a thin ZnO shell closely capping the PVAc core of the fiber. The ZnO shells uniformly covered the entire length and perimeter of the PVAc fibers, but their wall thickness was slightly asymmetrical due to shadowing effects as discussed below. Following calcination at 500 °C the organic (PVAc) fiber cores decomposed leaving only the inorganic (ZnO) shells. As a result, hollow ZnO fiber mats replicating the morphology of the as-spun PVAc fiber mats were produced, as shown in Figure 2c,d. The inner (bore) diameter of the ZnO hollow fibers varied between approximately 100 and 400 nm, slightly less than the diameter of the PVAc fibers in the as-spun state, displaying a small shrinkage that can be ascribed to densification of the ZnO shells following the decomposition of polymer fibers during the calcination step.

To examine the bottom part of fibers some pieces of calcined ZnO fiber mats were scratched off and removed from the substrate. SEM images of these scratched pieces show cracks along the bottom of the fibers, as demonstrated in Figure 2e. These cracks probably formed during the calcination step as a result of the high pressure that was built up inside the ZnO fibers due to thermal degradation of the PVAc fibers to volatile degradation products.[24] The internal pressure in

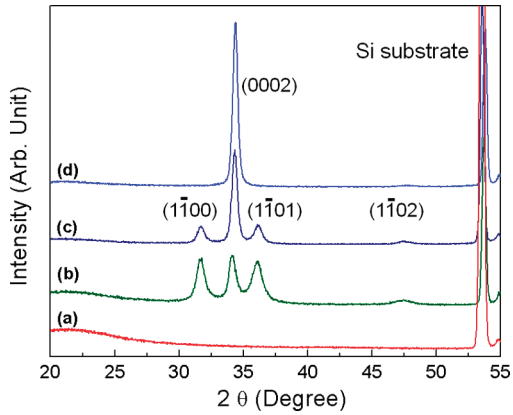

Figure 3. XRD diffractograms of (a) as-spun PVAc fibers; (b) after ZnO deposition by reactive sputtering; (c) after calcination at 500 °C; and (d) a reference ZnO film calcined at 500 °C.

the core of the fibers must have led to circumferential stresses in the ZnO shell in excess of its mechanical strength, ending up in cracking of the shell at the weakest point at the bottom of the shell where it is thinnest. Closer examination of the cross section of the ZnO fibers using focused ion beam (FIB) revealed elliptical tubular cross sections with asymmetrical wall thickness, as shown in Figure 2f. The wall thickness was largest at the top (105−107 nm), intermediate at the sidewalls (80−85 nm), and smallest at the bottom of the hollow fibers (37−47 nm). This asymmetry is attributed to the hydrodynamics of the fluxes of Zn^{2+} and O^{2-} ions sputtered from the ZnO ceramic target, accounting for partial shadowing introduced by the 3D morphology of the PVAc fiber template.[25] Compared to other PVD techniques such as thermal or electron-beam evaporation, sputter deposition is less influenced by such shadowing effects because the working pressure during deposition is typically higher giving rise to smaller mean free paths of the sputtered ions. As a result, the energetic ion fluxes encounter multiple scattering events before reaching the substrate, and therefore they are less affected by shadowing effects.

To examine the effect of shadowing on the morphology of different materials obtained by other deposition methods we used thermal evaporation to deposit Au overlayers onto our PVAc fiber templates. As shown in Figure 2g, the evaporated Au shells coated only the top section of the PVAc fibers, leaving part of their sidewalls and bottom completely uncoated. In comparison, the sputtered ZnO overlayers displayed much more uniform coating covering the entire circumference of the PVAc fibers (*cf.* Figure 2b). This demonstrates the directional nature of the evaporation process which is much more sensitive to shadowing effects compared to the relatively scattered nature of the sputter deposition process. Following calcination of the Au/PVAc composite fibers the polymer cores decomposed leaving their Au crusts unsupported. As a result the Au crusts crashed down to the substrate, leading to fragments of bended Au nanobelts as shown in Figure 2h. Combining all these steps sequentially, that is, electrospinning of PVAc fibers followed by sputtering the ZnO overlayer and then evaporating the Au crusts and finally calcination of the PVAc/ZnO/Au composite fibers, resulted in hollow ZnO fibers with Au crusts on their tops as shown in Figure 2i.

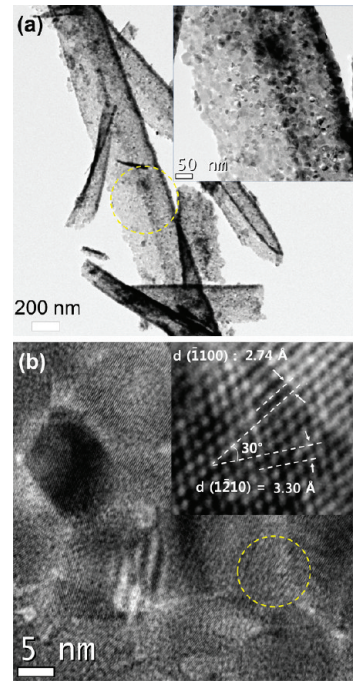

Figure 4. (a) TEM micrograph of a bunch of fragments of hollow ZnO fibers (the inset shows a high magnification TEM micrograph of the marked area). (b) HRTEM micrograph showing several ZnO nanocrystallites (the inset shows a magnified lattice image with the interplanar spacing corresponding to the (1$\bar{1}$10) and (1$\bar{2}$10) planes of the wurtzite structure marked in green and yellow, respectively).

The crystalline structure of the hollow ZnO fibers was examined by X-ray diffraction (XRD). Figure 3 shows representative X-ray diffractograms following different processing steps: (a) PVAc electrospinning; (b) ZnO sputtering; and (c) calcination; while the diffractogram in panel (d) corresponds to a reference ZnO film deposited by sputtering on a plain (untemplated) substrate and calcined under the same conditions as the templated layers. The as-spun PVAc fibers (spectrum a) were amorphous, as characterized by the broad peak centered around $2\theta \approx 20°$. The sputtered ZnO overlayers displayed polycrystalline wurtzite structure already in the as-deposited state (spectrum b). While no texture was observed in the as-deposited state, preferred (0002) orientation corresponding to the basal wurtzite plane oriented in parallel to the substrate was observed following calcination at 500 °C as evident from the strong (0002) reflection centered at $2\theta = 34°$ in the respective diffractogram (spectrum c). However, smaller peaks corresponding to (1$\bar{1}$00), (1$\bar{1}$01), and (1$\bar{1}$02) reflections still remained after the calcination step. In comparison, the reference ZnO film displayed only the

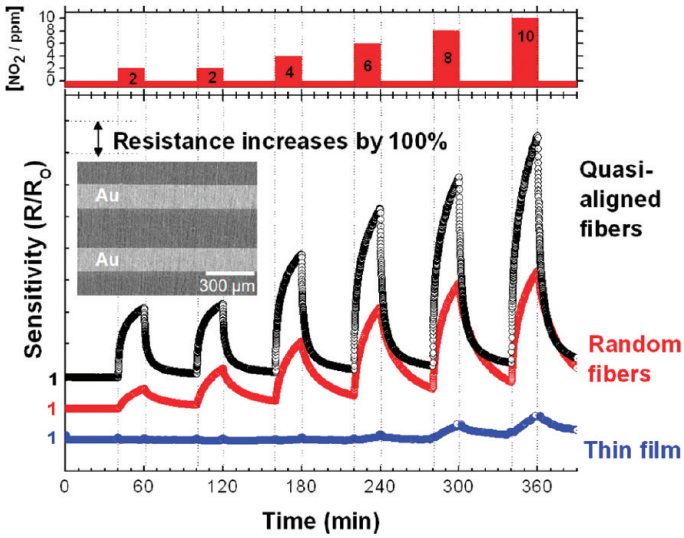

Figure 5. The resistance response R/R_0 (= I_0/I where I_0 is the baseline current in dry air at the beginning of the measurement and I is the DC current at time t during the measurement) during cyclic exposure to increasing NO_2 concentrations at 350 °C of sensors comprising a network of nonaligned (red) or quasi-aligned hollow ZnO fibers (black) and a reference ZnO thin film sensor (blue). Note that the responses of the three specimens are shifted vertically by one unit in order to separate them from each other. The NO_2 gas concentration profile is shown on top. The baseline current (I_0) levels were 6.0, 0.9, and 1.6 nA for the quasi-aligned fibers, nonaligned fibers, and thin film specimens, respectively. The inset shows a SEM micrograph of quasi-aligned fibers on an interdigitated alumina substrate, our prototypical sensor structure.

(0002) reflection (spectrum d), indicating strong preferential orientation of the basal wurtzite plane parallel to the substrate. The multiple ZnO reflections in spectrum c can therefore be ascribed to the curvature of the ZnO tubular shells bringing into Bragg's diffraction conditions the $(1\bar{1}00)$, $(1\bar{1}01)$, and $(1\bar{1}02)$ planes. The average crystallite size was obtained using the Scherrer equation, $D = 0.94\lambda/\beta \cos(2\theta)$, where D is the mean grain size, λ is the wavelength of the X-ray radiation ($\lambda = 0.154$ nm for Cu Kα radiation), and β is the full width at half-maximum of diffraction peak at 2θ, yielding $D \approx 23$ nm for the calcined ZnO hollow fibers.

To examine the microstructure of the hollow ZnO fibers in greater details, transmission electron microscopy (TEM) and high resolution transmission electron microscopy (HRTEM) characterizations were carried out. Figure 4 shows representative TEM micrographs of a bunch of hollow ZnO fibers. The low-magnification TEM image in Figure 4a shows the tubular shape of the hollow ZnO fibers, with diameters ranging from approximately 100 to 400 nm. The polycrystalline microstructure of the ZnO shells is clearly observed at higher magnifications, as shown in the TEM image in the inset of Figure 4a. High magnification HRTEM images such as the one shown in Figure 4b enabled direct grain size measurement of selected grains yielding grain size distribution between *ca.* 15 and 25 nm, in excellent agreement with the average grain size estimated from the peak broadening in the corresponding X-ray diffractogram (Figure 3c). Lattice images obtained at even higher magnifications displayed lattice fringes that can be identified with crystallographic planes of the ZnO wurtzite structure. For instance, lattice fringes having interplanar spacing of 2.46 and 3.30 Å with an angle of 30° between them, corresponding to ZnO $(1\bar{1}00)$ and $(1\bar{2}10)$ planes, respectively, are highlighted in the inset of Figure 4b.

To study the electronic transport properties and examine the gas sensing characteristics of the ZnO hollow fibers, DC conductivity and AC impedance spectroscopy measurements were carried out in different gas atmospheres. To this end nonaligned and quasi-aligned ZnO hollow fibers were deposited on alumina substrates fitted with interdigitated electrodes. The preparation method of these specimens followed the fabrication schemes depicted in Figure 1 panels a and b, respectively. An exemplary SEM micrograph of quasi-aligned fibers on an interdigitated alumina substrate is presented in the inset of Figure 5 showing an area with two gold electrodes (bright contrast) underneath the ZnO fibers, whereas the darker contrast corresponds to ZnO fibers covering the nonmetalized alumina substrate between the electrodes. In addition to nonaligned and quasi-aligned fibers, reference specimens comprising ZnO thin films (~200 nm thick) deposited directly onto interdigitated alumina substrates without the polymer templates were prepared and measured under the same conditions as their hollow fiber counterparts for comparison purposes.

Representative results of the resistance response of three exemplary specimens during cyclic exposures to increasing NO_2 concentrations at 350 °C are shown in Figure 5. The hollow fibers were considerably more sensitive than their thin film counterparts, displaying well resolved response signals down to the lowest NO_2 concentration (2 ppm) experienced in our tests. In contrast, the thin film reference sensors did not show a de-

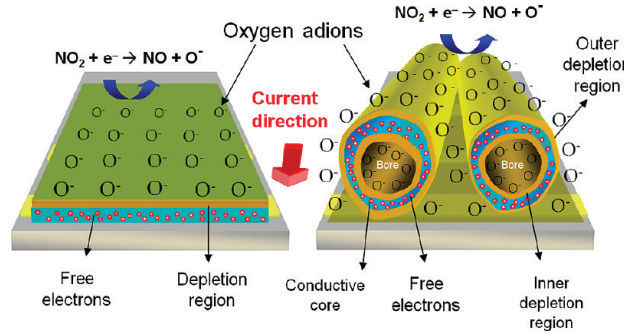

Figure 6. Schematic cartoons showing the effect of NO_2 adsorption on the electronic transport properties of ZnO planar thin films (left cartoon) and aligned hollow fibers (right cartoon).

tectable response below 8 ppm, and their sensitivity (at higher concentrations) was considerably smaller compared to the hollow fiber sensors. The enhanced gas sensitivity of the hollow fibers can be attributed, in part, to their high surface to volume ratio. Note that gas molecules can reach not only the outer but also the inner surface of the hollow ZnO fibers *via* the cracks at the bottom of the fibers (see Figure 2e). The sensitivity of nanostructured metal−oxide gas sensors scales with the surface to volume ratio.[26,27] Therefore, given the fact that this ratio is twice as large for hollow fibers as for planar films of the same thickness,[28] their sensitivity is expected to be enhanced by a factor of 2 based on this geometric consideration alone. However, as demonstrated in Figure 5 the sensitivity of our hollow fiber sensors was found to be much higher than their thin film counterparts, outshining this 2-fold enhancement by far and large. This suggests that other effects may have led to further enhancement in sensitivity.

The high resistance surface depletion regions and relatively conductive cores of the thin film and hollow fiber sensors are depicted schematically in Figure 6. The surface depletion regions, whose thickness and resistivity vary as a function of the gas composition due to adsorption of electronegative gases such as NO_2 (see discussion below), are shown in green while the remaining relatively conductive cores are in blue. Further enhancement of the gas sensitivity of the hollow fibers compared to their thin film counterparts above and beyond the 2-fold "geometric" enhancement due to the 2-fold increase in their surface-to-volume ratio may result from nontrivial effects connected with their unique morphology and unusual electronic transport properties. Such effects may include, for instance, constriction of the current to the conductive cores of the fibers giving rise to 1D transport phenomena. As a result, the free carriers (electrons) must tunnel through every local barrier introduced by gas adsorption along the entire length of the fiber from one electrode to the next. This so-called molecular wire effect is responsible for the ultrahigh sensitivity of chemical sensors based on 1D polymer chains.[29] In contrast, in the thin film case the current flow is 2D and therefore it can percolate around these barriers mitigating their influence on the overall film resistance. Likewise, deleterious effects such as interdiffusion, solid state reaction, and the so-called "dead layer" effect[30] connected with the interface between the sensing layer and the substrate are significantly mitigated in fibrillar scaffolds because the interface area between the fibers and the substrate is so small (*cf.* Figure 2d).

Between the quasi-aligned and nonaligned hollow fibers, the former demonstrated approximately 2-fold higher sensitivity. The sensitivity enhancement of the quasi-aligned fibers may result from a number of different reasons including improved gas transport properties and more distinctive 1D character of the electronic transport along the aligned fibers compared to their non-

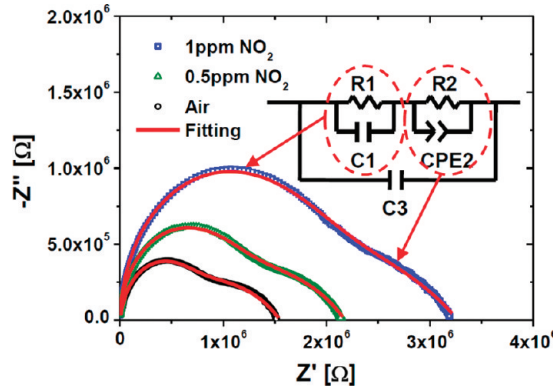

Figure 7. Impedance spectra of a quasi-aligned hollow ZnO fiber specimen (the same specimen as in Figure 5, black curve) under steady state conditions in clean air or air mixed with 0.5 or 1 ppm NO_2 at 400 °C. The inset shows the equivalent circuit used for fitting the experimental data.

aligned counterparts wherein the current may take percolation paths crossing from one fiber to another avoiding local barriers similarly to the thin film case. Further investigations should be carried out to clarify the electronic transport and gas sensing mechanisms of aligned versus nonaligned fibers but all the same the observation that the aligned fibers were considerably more sensitive than their nonaligned counterparts is encouraging, demonstrating that significant improvement in gas sensing properties can be achieved using fiber alignment techniques.

All our specimens displayed higher resistances upon exposure to NO_2 compared to the baseline resistance in clean air (*cf.* Figure 5), regardless of their morphology and microstructure, test temperature, and NO_2 concentration. This observation is in agreement with previous reports[31,32] that ZnO typically behaves as an *n*-type semiconducting metal−oxide whose surface conductivity typically decreases upon exposure to electronegative gases such as NO_2 due to electron localization at surface adsorbates.[33] This arises from the high electron affinity of the NO_2 molecules leading to electron transfer from the ZnO layer to surface adsorbates. On the basis of recent density functional theory (DFT) calculations, the adsorption of NO_2 on ZnO nanotubes leads to dissociation to NO and O^- following the reaction $NO_2 + e^- \rightarrow NO + O^-$.[34] The resultant O^- adions add up to the preadsorbed O^- adions that already exist at the surface due to chemisorption of oxygen from the air,[35] increasing the width of the depletion region and the sensor resistance as a result of enhanced electron localization at O^- adions introduced by the surface reaction with NO_2. As can be seen in Figure 5 the response was reversible despite the fact that steady state conditions were not achieved due to insufficient exposure time (20 min). The fact that both the hollow fibers and thin film specimens did not reach steady state suggests that the reaction kinetics was limited by surface rather than gas transport processes although further investigations should be carried out to verify this conclusion.

TABLE 1. Equivalent Circuit Fit Values for the Impedance Spectra in Figure 7

	air	0.5 ppm NO_2	1 ppm NO_2
R1 [Ω]	5.1×10^5	9.3×10^5	1.4×10^6
C1 [F]	4.3×10^{-12}	1.9×10^{-12}	1.5×10^{-12}
R2 [Ω]	1.1×10^6	1.3×10^6	1.9×10^6
Q_0 [Fs^{n-1}]	9.1×10^{-9}	8.9×10^{-9}	9.6×10^{-9}
n	0.49	0.49	0.44
ω_{max} [rad/s]	205247	126776	85809
C2[a] [F]	1.7×10^{-11}	2.3×10^{-11}	1.7×10^{-11}
C3 [F]	2.1×10^{-12}	3.4×10^{-12}	3.7×10^{-12}
χ^2	0.00050	0.00047	0.00059

[a] C2 was calculated using the formula $C = Q_0 \times \omega_{max}^{n-1}$.

To examine the electronic transport properties of the quasi-aligned hollow fibers in more details and obtain further insight into their NO_2 gas sensing mechanism, impedance spectroscopy measurements were carried out under similar temperatures and gas compositions as in our gas sensing tests. Figure 7 shows impedance spectra of the same quasi-aligned fibers specimen whose gas sensing results are shown in Figure 5. The impedance spectra were measured at 400 °C in clean air or air mixed with 0.5 or 1 ppm NO_2. The results are presented in complex impedance plane plots (also known as Cole−Cole or Nyquist plots) in which the (negative value of the) imaginary impedance ($-Z''$) is plotted against the real impedance (Z'). In this presentation two distinct semicircles were obtained, as shown in Figure 7, corresponding to different contributions to the overall impedance of the sensor. These contributions are characterized by different relaxation times, $\tau = \rho\epsilon$ (ρ = resistivity, ϵ = permittivity), that give rise to separate semicircles in the complex impedance plane. The semicircle on the left of each spectrum (close to the origin) corresponds to high frequencies (small τ), whereas the one on the right corresponds to low frequencies (large τ). Typically they represent the dielectric response of the bulk material and interfacial (double layer) phenomena, respectively.[36]

The impedance spectra in Figure 7 can be fitted quite well with an equivalent circuit comprising two parallel RC (R, resistor; C, capacitor) units connected in series and a third parallel capacitor, as depicted in the inset of Figure 7. The first and third capacitors (C1 and C3) were found to be ideal capacitors, while the second one (C2) was best fitted with a constant phase element (CPE) because the corresponding semicircles (the ones on the right-hand side of each spectrum) were depressed (*i.e.*, their centers lay below the *x*-axis). Constant phase elements are often used to describe the behavior of polycrystalline materials or electrochemical systems having a distribution of some of their electrical properties (*e.g.*, grain boundary or electrode resistance) that give rise to a distribution of the respective relaxation time τ. The impedance of a constant phase element is given by $Z_{CPE} = 1/[Q_0(j\omega)^n]$, where Q_0 is the admittance at $\omega = 1$ rad/s (having dimension of Fs^{n-1}) and n is a positive dispersion parameter smaller than unity.[35] The respective values of the equivalent circuit elements obtained by fitting the impedance spectra in Figure 7 to the equivalent circuit shown in the inset of the figure and the goodness of fit parameter (χ^2) are listed in Table 1. The low values of C1 and C3 are indicative of bulk contributions to the overall impedance while the relatively high value of C2 suggests an interfacial contribution.[36,37] On the basis of these observations and considering the specimen's morphology and microstructure, we assign C3 to the depletion regions in the inner and outer surfaces of the hollow ZnO fibers (*cf.* the green regions on the right cartoon in Figure 6). Being depleted of mobile charge carriers (electrons) these regions were highly resistive and their contribution to the conductivity was negligible. Consequently, the current was constricted to the cores of the hollow fibers (*cf.* the blue regions on the right cartoon in Figure 6). The resistive and capacitive contributions of these conductive cores to the overall impedance of the hollow fibers are represented by the equivalent circuit elements R1 and C1, respectively. We note that the values of C1 and C3 are quite close (*cf.* Table 1), supporting the assignment of the respective equivalent circuit elements to the core and shells (inner and outer shells) of the hollow fibers, respectively.

The relatively high value of C2 and the fact that it fits much better a constant phase element with a low dispersion parameter ($n \approx 0.5$) rather than an ideal capacitor ($n = 1$) suggests that the respective element (R2//CPE2) in the equivalent circuit is connected with interfacial contribution to the overall impedance. The origin of this interfacial contribution is not entirely clear yet and we can only speculate that it may be connected with the contribution of the grain boundaries in the nanocrystalline hollow fibers (*cf.* Figure 4) or perhaps with the semiconductor/metal contacts between the ZnO hollow fibers and the interdigitated gold electrodes. Note that both R1 and R2 increased on exposure to NO_2, but R1 was considerably more sensitive than R2. Further investigations should be carried out to clarify the origin of the interfacial contribution and its effect on the gas sensing mechanism.

In summary, we presented a new processing method for the fabrication of unique device architectures comprising hollow fibers of inorganic materials with typical length of up to several centimeters, submicrometer diameter, and wall thickness of several tens of nanometers. The hollow fibers can be assembled in different ways enabling the construction of nanoengineered device architectures with tailored functional properties. Using this fabrication method we prepared quasi-aligned or random networks of hollow ZnO fibers and investigated their microstructure evolution and electronic transport properties. DC conductivity and AC impedance spectroscopy measurements in clean air or under exposure to residual concentrations of NO_2 revealed that the inner and outer surfaces of the hollow ZnO fibers were depleted of mobile charge carri-

ers, constricting the current to flow through their less resistive cores. This current constriction gave rise to 1D electronic transport along the hollow fibers, which might be the reason for the unexpectedly large enhancement in their gas sensitivity compared to reference thin film specimens of the same composition (ZnO) and thickness. Compared to previous reports on gas sensors produced by electrospinning techniques our hollow ZnO fibers are considerably more sensitive than solid fibers of MoO_3 or WO_3 produced by the electrospinning of polymer fibers containing inorganic precursors of Mo or W, respectively.[38] Although they are not as sensitive as mesoporous TiO_2 fibers produced by electrospinning followed by hot-pressing and calcination steps,[39] the process presented in this work does not involve hot-pressing and therefore it may be more compatible with low power sensor arrays (so-called *electronic nose*) fabricated on microhot plate platforms.[40]

METHODS

Sample Preparation. Polyvinyl-acetate (PVAc) fibers were electrospun from a solution of dimethylformamide (DMF, 16.5 mL), PVAc (0.75 g, M_w = 1 300 000 g/mol) and cetyltrimethylammonium bromide (CTAB, 0.05 g). DMF was used as a solvent and CTAB as an organic salt to increase the electrical conductivity of the solution. In the electrospinning process the solution was injected through a stainless steel needle (21 gauge, orifice diameter = 300 μm) that was connected to a high-voltage DC power supply (Bertan, High Voltage Power Supply series 230). The solution was continuously fed through the nozzle using a syringe pump (KD scientific, 781200) at a rate of 10 μm/min. High voltage (13 kV) was applied between the needle and the grounded collector 11 cm below it. As a result, a continuous stream was ejected from the nozzle as a long fiber and collected on the substrates. Silicon wafers were used as substrates in specimens for microstructural characterizations and polycrystalline alumina ceramic substrates fitted with interdigitated electrodes (16 fingers, 8 mm long and 200 μm wide, spaced 200 μm apart) comprising 200 nm thick gold electrodes on a 50 nm thick titanium adhesion layer, which were used for electrical and gas sensing measurements. To obtain uniaxial alignment of the fibers, two stripes of aluminum wires (diameter = 0.5 mm) were placed right next to the substrate edges in parallel to the interdigitated electrodes as shown in Figure 1b and connected to the ground terminal of the power supply. The distribution of the electrical field flux lines between the needle and the aluminum wires led to uniaxial alignment of the electrospun fibers perpendicular to the wires and the interdigitated electrodes. Following the electrospinning process a thin overlayer (approximately 100 nm thick) of ZnO was sputtered onto the PVAc fiber template covering the substrate. The ZnO layer was sputtered from a ZnO target (99.999% pure) using rf power of 100 W under a flow of Ar (10 sccm) at a working pressure of 60 mTorr. The substrates were not heated during sputtering to prevent thermal decomposition of the PVAc template. Subsequently, the samples were calcined at 500 °C for 1 h to remove the polymer template by thermal decomposition of the organic components and to crystallize the inorganic (ZnO) overlayers.

Material Characterizations. The morphology and microstructure evolution of the fibers were examined after each processing step by means of field emission scanning electron microscopy (SEM, JEOL JSM 6330F). Focused ion beam (FIB, Nova 600, FEI) was used, in some cases, to cut sharp cross sections of the hollow ZnO fibers for closer examination of their cross section structure. Thermogravimetric/differential thermal analysis (TG/DTA) were carried out using a TG2050 thermal analyzer system (Ta instrument, Inc.) to examine the thermal degradation of the organic components in the ZnO-coated PVAc fibers. The crystalline structure was examined by X-ray diffraction (XRD) using a Rigaku D/MAX-RC diffractometer with Cu Kα radiation, and the microstructure was observed by means of transmission electron microscopy (TEM) and high resolution transmission electron microscopy (HRTEM) using a FEI Tecnai G2 microscope. Sample preparation of TEM specimens involved ultrasonication to disperse the hollow ZnO fibers in ethanol followed by immobilizing the suspension on a carbon-coated copper grid.

Gas Sensing Tests. Gas sensing tests were carried out by monitoring changes in the DC current (using Keithley 6514 electrometer) under constant applied voltage (50 mV) during cyclic exposure to trace concentrations (between 2 and 10 ppm) of NO_2 in dry air. To achieve this, a premixed NO_2/air gas mixture containing 50 ppm of NO_2 in dry air (BOC U.K.) was mixed with clean dry air using mass flow controllers (MKS). To ensure that the residual concentrations of NO_2 and other interfering gases in the reference gas (air) were well below the minimum exposure level (2 ppm) of the test gas (NO_2), we passed fresh air through a zero air generator (Environics series 7000 Zero Air Generator) comprising catalytic converter and Purafil and Charcoal scrubbers. The zero air generator is specified by the manufacturer to provide dry air (dew point < -10 °C) with residual concentration of less than 0.5 ppb for NO, NO_2, SO_2, and O_3 and less than 25 ppb for hydrocarbons and CO. The gas sensing and impedance spectroscopy measurements were carried out in a small (~0.5 L) cylindrical UHV-compatible stainless steel chamber fitted with gas inlet and outlet ports and a temperature-controlled specimen holder (hot stage). The measurements were carried out in the temperature range 200−400 °C taking the necessary measures to ensure stable and reproducible baseline at the beginning of each test. To this end the specimens were equilibrated under the baseline conditions, that is in clean air, at the test temperature for several hours (typically around 12 h) prior to the exposure to the test gas (NO_2).

Impedance Spectroscopy Measurements. The impedance spectra were measured at 400 °C in clean air or air mixed with 0.5 or 1 ppm NO_2. The complex impedance $Z(\omega) = Z'(\omega) - jZ''(\omega)$ was measured as a function of frequency ($f = 2\pi/\omega$) between 1 Hz and 1 MHz with an ac amplitude (V_{ac}) of 20 mV using a frequency response analyzer (Novocontrol Alpha-AK) coupled to an electrochemical test interface (Novocontrol POT/GAL). Upon changing the gas atmosphere (that is, the NO_2 concentration) sufficient time was given for the specimen to reach stable steady state conditions as determined by monitoring the complex impedance (at f = 1 Hz) as function of time. The respective stabilization times were on the order of few hours, considerably longer than the exposure time (20 min) in the gas sensing tests (*cf.* Figure 5).

Acknowledgment. This work is dedicated to Professor Harry Tuller on his 65th anniversary. This research was supported by a grant from the Ministry of Research, Korea, and the Ministry of Science, Culture & Sport, Israel, and KIST program under Grant No. 2E21400. A.R. acknowledges the support of the Russell Berrie Nanotechnology Institute (RBNI) and the Wolfson Family Charitable Trust. A.R. holds the Horev fellowship for leaders in science and technology—supported by the Taub Foundation.

REFERENCES AND NOTES

1. Zheng, Q.; Zhou, B.; Bai, J.; Li, L.; Jin, J.; Zhang, J.; Li, J.; Liu, Y.; Cai, W.; Zhu, X. Self-Organized TiO_2 Nanotube Array Sensor for the Determination of Chemical Oxygen Demand. *Adv. Mater.* **2008**, *20*, 1044–1049.
2. Varghese, O. K.; Gong, D.; Paulose, M.; Ong, K. G.; Dickey, E. C.; Grimes, C. A. Extreme Changes in the Electrical Resistance of Titania Nanotubes with Hydrogen Exposure. *Adv. Mater.* **2003**, *15*, 624–627.

3. Kim, I. D.; Rothschild, A.; Hyodo, T.; Tuller, H. L. Microsphere Templating as Means of Enhancing Surface Activity and Gas Sensitivity of $CaCu_3Ti_4O_{12}$ Thin Films. *Nano Lett.* **2006**, *6*, 193–198.
4. Kim, I. D.; Rothschild, A.; Yang, D. J.; Tuller, H. L. Macroporous TiO_2 Thin Film Gas Sensors Obtained Using Colloidal Templates. *Sens. Actuators B* **2008**, *130*, 9–13.
5. Rolison, D. R. Catalytic Nanoarchitectures—The Importance of Nothing and the Unimportance of Periodicity. *Science* **2003**, *299*, 1698–1701.
6. Shankar, K.; Bandara, J.; Paulose, M.; Wietasch, H.; Varghese, O. K.; Mor, G. K.; LaTempa, T. J.; Thelakkat, M.; Grimes, C. A. Highly Efficient Solar Cells using TiO_2 Nanotube Arrays Sensitized with a Donor-Antenna Dye. *Nano Lett.* **2008**, *8*, 1654–1659.
7. Yang, S. C.; Yang, D. J.; Kim, J.; Hong, J. M.; Kim, H. G.; Kim, I. D.; Lee, H. Hollow TiO_2 Hemispheres Obtained by Colloidal Templating for Application in Dye-Sensitized Solar Cells. *Adv. Mater.* **2008**, *20*, 1059–1064.
8. Mor, G. K.; Varghese, O. K.; Wilke, R. H. T.; Sharma, S.; Shankar, K.; Latempa, T. J.; Choi, K. S.; Grimes, C. A. p-Type Cu-Ti-O Nanotube Arrays and Their Use in Self-Biased Heterojunction Photoelectrochemical Diodes for Hydrogen Generation. *Nano Lett.* **2008**, *8*, 1906–1911.
9. Futaba, D. N.; Hata, K.; Yamada, T.; Hiraoka, T.; Hayamizu, Y.; Kakudate, Y.; Tanaike, O.; Hatori, H.; Yumura, M.; Iijima, S. Shape-Engineerable and Highly Densely Packed Single-Walled Carbon Nanotubes and Their Application as Super-Capacitor Electrodes. *Nat. Mater.* **2006**, *5*, 987–994.
10. Ben-Jacob, E.; Hanein, Y. Carbon Nanotube Micro-Electrodes for Neuronal Interfacing. *J. Mater. Chem* **2008**, *18*, 5181–5186.
11. Yi, G.-R.; Moon, J. H.; Yang, S. M. Ordered Macroporous Particles by Colloidal Templating. *Chem. Mater.* **2001**, *13*, 2613–2618.
12. Correa-Duarte, M. A.; Maceira, V. S.; Rodriguez-Gonzalez, B.; Liz-marzan, L. M.; Kosiorek, A.; Kandulski, W.; Giersig, M. Asymmetric Functional Colloids through Selective Hemisphere Modification. *Adv. Mater.* **2005**, *17*, 2014–2018.
13. Chen, J.; McLellan, J. M.; Siekkinen, A.; Xiong, Y.; Li, Z-Y; Xia, Y. Facile Synthesis of Gold−Silver Nanocages with Controllable Pores on the Surface. *J. Am. Chem. Soc.* **2006**, *128*, 14776–14777.
14. Grimes, C. A. Synthesis and Application of Highly Ordered Arrays of TiO_2 Nanotubes. *J. Mater. Chem.* **2007**, *17*, 1451–1457.
15. Özgür, Ü.; Alivov, Y. I.; Liu, C.; Teke, A.; Reshchikov, M. A.; Doğan, S.; Avrutin, V.; Cho, S.-J.; Morkoç, H. A Comprehensive Review of ZnO Materials and Devices. *J. Appl. Phys.* **2005**, *98*, 041301(1−103).
16. Reneker, D. H.; Yarin, A. L.; Zussman, E. Electrospinning of Nanofibers from Polymer Solutions and Melts. *Adv. Appl. Mech.* **2007**, *41*, 43–195.
17. Ramaseshan, R.; Sundarrajan, S.; Jose, R.; Ramakrishna, S. Nanostructured Ceramics by Electrospinning. *J. Appl. Phys.* **2007**, *102*, 111101(1−17).
18. Sigmund, W.; Yuh, J.; Park, H.; Maneeratana, V.; Pyrgiotakis, G.; Daga, A.; Taylor, J.; Nino, J. C. Processing and Structure Relationships in Electrospinning of Ceramic Fiber Systems. *J. Am. Ceram. Soc.* **2006**, *89*, 395–407.
19. McCann, J. T.; Li, D.; Xia, Y. Electrospinning of Nanofibers with Core−Sheath, Hollow, or Porous Structures. *J. Mater. Chem.* **2005**, *15*, 735–738.
20. Sun, D.; Chang, C.; Li, S.; Lin, L. Near-Field Electrospinning. *Nano Lett.* **2006**, *6*, 839–842.
21. Peng, Q.; Sun, X.-Y.; Spagnol, J. C.; Hyde, G. K.; Spontak, R. J. Parsons, G. N. Atomic Layer Deposition on Electrospun Polymer Fibers as a Direct Route to Al_2O_3 Microtubes with Precise Wall Thickness Control. *Nano Lett* **2007**, *7*, 719–722.
22. Ochanda, F.; Jone, W. E., Jr. Fabrication and Thermal Analysis of Submicron Silver Tubes Prepared from Electrospun Fiber Templates. *Langmuir* **2007**, *23*, 795–801.
23. Li, D.; Wang, Y.; Xia, Y. Electrospinning of Polymeric and Ceramic Nanofibers as Uniaxially Aligned Arrays. *Nano Lett.* **2003**, *3*, 1167–1171.
24. Zussman, E.; Yarin, A. L.; Bazilevsky, A. V.; Avrahami, R.; Feldman, M. Electrospun Polyacrylonitrile/Poly(methyl methacrylate)-Derived Turbostratic Carbon Micro-/Nanotubes. *Adv. Mater.* **2006**, *18*, 348–353.
25. Mayo, A. A.; Hamaguchi, S.; Joo, J. H.; Rossnagel, S. M. Across-Wafer Nonuniformity of Long Throw Sputter Deposition. *J. Vac. Sci. Technol., B* **1997**, *15*, 1788–1793.
26. Rothschild, A.; Komem, Y. On the Relationship Between the Grain Size and Gas-Sensitivity of Chemo-resistive Metal−Oxide Gas Sensors with Nanosized Grains. *J. Electroceram.* **2004**, *13*, 697–701.
27. Rothschild, A.; Komem, Y. The Effect of Grain Size on the Sensitivity of Nanocrystalline Metal−Oxide Gas Sensors. *J. Appl. Phys.* **2004**, *95*, 6374–6380.
28. This is simply due to the fact that both the inner and outer surfaces of the hollow fibers are exposed to the gas phase, whereas in the thin film case only the outer surface is in contact with the gas phase (the inner surface being the interface with the substrate).
29. Swager, T. M. The Molecular Wire Approach to Sensory Signal Amplification. *Acc. Chem. Res.* **1998**, *31*, 201.
30. Rothschild, A.; Tuller, H. L. Gas sensors: New Materials and Processing Approaches. *J. Electroceram.* **2006**, *17*, 1005.
31. Min, Y.; Tuller, H. L.; Palzer, S.; Wöllenstein, J.; Böttner, H. Gas Response of Reactively Sputtered ZnO Films on Si-Based Micro-array. *Sens. Actuators, B* **2003**, *93*, 435–441.
32. Kobrinsky, V.; Rothschild, A.; Lumelsky, V.; Komem, Y.; Lifshitz, Y. Tailoring the Gas Sensing Properties of ZnO Thin Films through Oxygen Nonstoichiometry. *Appl. Phys. Lett.* **2008**, *93*, 113502(1−3).
33. Williams, D. E. Semiconducting Oxides as Gas-Sensitive Resistors. *Sens. Actuators, B* **1999**, *57*, 1–16.
34. An, W.; Wu, X.; Zeng, X. C. Adsorption of O, H, CO, NH, and NO on ZnO Nanotube: A Density Functional Theory Study. *J. Phys. Chem. C* **2008**, *112*, 5747–5755.
35. Rothschild, A.; Komem, Y. Numerical Computation of Chemisorptions Isotherms for Device Modeling of Semiconductor Gas Sensors. *Sens. Actuators, B* **2003**, *93*, 362–369.
36. Barsoukov, E.; Macdonald, J. R. *Impedance Spectroscopy: Theory, Experiment, and Applications*, 2nd edition; Wiley: Hoboken, NJ, 2005.
37. Kim, I. D.; Rothschild, A.; Tuller, H. L. Direct Current Bias Effects on Grain Boundary Schottky Barriers in $CaCu_3Ti_4O_{12}$. *Appl. Phys. Lett.* **2006**, *88*, 72902(1−3).
38. Sawicka, K. M.; Prasad, A. K.; Gouma, P. I. Metal Oxide Nanowires for Use in Chemical Sensing Applications. *Sens. Lett.* **2005**, *3*, 31–35.
39. Kim, I. D.; Rothschild, A.; Lee, B. H.; Kim, D. Y.; Jo, S. M; Tuller, H. L. Ultrasensitive Chemiresistors Based on Electrospun TiO_2 Nanofibers. *Nano Lett.* **2006**, *6*, 2009–2013.
40. Semancik, S.; Cavicchi, R. E.; Wheeler, M. C.; Tiffany, J. E.; Poirier, G. E.; Walton, R. M.; Suehle, J. S.; Panchapakesan, B.; DeVoe, D. L. Microhotplate Platforms for Chemical Sensor Research. *Sens. Actuators, B* **2001**, *77*, 579–591.